

Report Title

Advance ratio effects on the dynamic-stall vortex of a rotating blade in steadyforward ight

ABSTRACT

The effect of advance ratio on the flow structures above a rotor blade in dynamic stall is studied using stereoscopic particle image velocimetry. The dynamic stall vortex shows a significant velocity component in its core, implying a helical structure progressing radially outboard. The radial velocity attenuates at outboard locations, in contrast to the expected increase with centripetal acceleration. This attenuation is accompanied by an increase in unsteadiness of the vortex. The unsteadiness shows a low-frequency cycle-to-cycle variation despite steady freestream conditions and blade tracking. Proper orthogonal decomposition analysis of the dominant flow mode confirms the unsteady behavior of the leading-edge vortex. The dependence on advance ratio is used to relate the stability of the dynamic-stall vortex to Coriolis effects.

Advance ratio effects on the dynamic-stall vortex of a rotating blade in steady forward flight

Vrishank Raghav^{1, a)} and Narayanan Komerath^{1, b)}

School of Aerospace Engineering, Georgia Institute of Technology, 270 Ferst Drive, Atlanta, GA 30332, USA

(Dated: 6 August 2014)

The effect of advance ratio on the flow structures above a rotor blade in dynamic stall is studied using stereoscopic particle image velocimetry. The dynamic stall vortex shows a significant velocity component in its core, implying a helical structure progressing radially outboard. The radial velocity attenuates at outboard locations, in contrast to the expected increase with centripetal acceleration. This attenuation is accompanied by an increase in unsteadiness of the vortex. The unsteadiness shows a low-frequency cycle-to-cycle variation despite steady freestream conditions and blade tracking. Proper orthogonal decomposition analysis of the dominant flow mode confirms the unsteady behavior of the leading-edge vortex. The dependence on advance ratio is used to relate the stability of the dynamic-stall vortex to Coriolis effects.

Keywords: Leading-edge vortex, Dynamic stall vortex, Vortex flows, Rotating wing

^{a)}Electronic mail: vrishank@gatech.edu

^{b)}Electronic mail: komerath@gatech.edu

I. INTRODUCTION

The aerodynamic loading and associated flow structure on rotating wings and blades has been of great interest for several decades now with applications to wind turbines, compressors, helicopter rotors, and even insect wing aerodynamics. Dynamic stall occurs on rotating blades of a helicopter in forward flight, on the retreating blade side where the pitch angle is increased to balance the rolling moment on the vehicle. This unsteady flow field is characterized by the roll-up of the leading-edge shear layer into a coherent and three-dimensional dynamic-stall vortex (DSV also commonly known as the leading-edge vortex (LEV)) and its subsequent shedding. Although the conditions at which the vortex is formed in each case is different, the flow structure and physics of the DSV is quite similar between the different situations. Dickson¹ and Lentink² briefly discuss the similarities and differences between the flow structure on helicopter rotor blades, wind turbine blades, and insect wings. Due to these wide engineering implications there has been a continuing interest in understanding the flow structure and dynamics of the DSV/LEV on rotating wings.

Studies investigating the velocity field on helicopter rotors³⁻⁵ and wind turbine blades⁶⁻⁸ have shown the existence of a three-dimensional DSV, while similar flow structures have also been observed on rotating insect wing investigations^{2,9-13}. A common theme among most of these investigations is the existence of a strong span-wise flow from wing root-to-tip (hereafter referred to as radial flow) on the associated rotating wing. Often, this radial flow has been observed to play a critical role in the dynamics of the vortex with several investigations addressing its role in the stabilization of the vortex. Rotating wings setup to operate as helicopter rotor blades have studied effects of radial flow on the characteristics of the DSV^{3,5}. Mulleners³ observed only small cycle-to-cycle variations of the DSV, and hypothesized that the “radial forcing” due to rotating effects was stabilizing the DSV. Furthermore, Mulleners’s results corroborated observations by Raghav¹⁴ that the radial flow on a rotating blade under dynamic stall conditions attenuated upon moving outboard towards the tip of the blade. The physical mechanism for this phenomenon was ascertained by Raghav to be an apparent shear layer instability of the radial flow.

Hitherto, most studies have been conducted at hovering flight conditions. In contrast to the case of a fixed pitch wing rotating in quiescent fluid (hovering flight conditions), limited studies exist which address the effect of steady incident flow (climbing/forward flight conditions). Several researchers have experimentally and numerically investigated the flow field over helicopter blades in hover conditions¹⁵⁻¹⁷. Recently, Bross¹⁸ conducted experiments to study the effect of

incident steady flow at low Reynolds numbers, whereby the direction of flow was along the axis of rotation (climbing flight conditions, similar to wind turbine in steady freestream at zero yaw). Bross et al. observed that the development of the flow structure in the leading edge region was relatively insensitive to advance ratio (climbing flight condition). Dickson¹ studied the effect of steady incident tangential flow (forward flight conditions) on the aerodynamic loads on a rotating wing with *fixed pitch* at low Reynolds numbers. However, Dickson did not investigate the nature and structure of the flow field in forward flight conditions. To the authors' knowledge, no studies have been directed towards the effect of advance ratio during forward flight conditions on the flow structure of a wing undergoing simultaneous rotation and pitching. Although the problem defined here is well known in the rotorcraft community, only a few studies investigate the flow structure on simultaneously rotating and pitching wings³⁻⁵, and *none* address the effect of advance ratio during forward flight.

In this work stereoscopic particle image velocimetry (SPIV) measurements are used to bridge this gap in knowledge of the flow structure by studying the flow field over a low aspect-ratio wing. The data were acquired after several hundred rotations of the wing to ensure steady state rotation with no effect of rotational acceleration. The measurements are acquired at one specific azimuth of $\psi = 270^\circ$ (see Fig. 1a for definition of ψ) and three radial locations at this azimuth. Given the flow conditions, this choice of azimuth $\psi = 270^\circ$ serves two purposes: a) it is the azimuth where the combination of flow conditions and angle of attack leads to the formation of a DSV via the dynamic stall mechanism, and b) it allows for a systematic study of the effect of advance ratio on the radial flow, by focusing on the azimuthal location where centripetal acceleration induced radial flow is expected to dominate the flow field. The measurements at different radial locations help in understanding the span-wise variations of the DSV.

The main objectives of the study presented herein were to investigate the effect of advance ratio and radial location on the DSV of a rotating wing in steady incident tangential flow. The SPIV velocity field measurements are used to ascertain its variation in structure and location with advance ratio and radial location. The variations in the vortex strength with advance ratio are quantified using circulation estimates. Furthermore, the effect of advance ratio on the radial flow is studied while the rotation rate is held constant. In addition to phase-averaged analysis, instantaneous velocity field analysis is performed to quantify the cycle-to-cycle variations. Proper orthogonal decomposition technique is used to study the dominant flow mode and draw conclusions on the unsteadiness of the DSV. Finally, the stability of the DSV is discussed in the context of the radial

flow and advance ratio of the blade.

II. EXPERIMENTAL METHODS

A. Experimental setup and flow conditions

The experiments were conducted in the closed atmospheric pressure test section of the John Harper 2.13 m \times 2.74 m low speed wind tunnel at the Georgia Institute of Technology. The closed circuit tunnel is powered by a three-phase 600 hp induction motor controlled by a variable frequency drive, with the error in fan angular velocity maintained below 0.1%. The freestream longitudinal turbulence intensity at the entrance of the empty test section was 0.06% measured at a freestream velocity of 34 m s⁻¹. The longitudinal turbulence intensity reported here was computed from velocity fluctuations data acquired using a hot-film conditioned with a 3 Hz high pass filter and 2.5 kHz low pass filter.

The experimental setup, the high advance ratio facility, was fabricated in the test section of the wind tunnel and is illustrated in Fig. 1. In order to simplify the operations, a two-bladed rotor design was preferred. The setup had manually adjustable collective and cyclic pitch control settings, which was achieved by using a swashplate (please refer to Johnson¹⁹ for details of a swashplate mechanism). In addition, a photo-micro sensor was installed on the rotor shaft to enable phase locked data measurement. A rectangular, untwisted wing with a NACA0013 airfoil profile was used in this investigation. The wing has an aspect ratio $AR = 3.49$, a chord $c = 178$ mm, a span $b = 622$ mm. The radial distance from the axis of rotation is represented by r and has values of $R_o = 267$ mm and $R = 889$ mm, at the root and tip of the wing respectively. Further details of the rotor specifications and experimental setup are provided in Raghav⁵.

Given the objectives and motivation of this study, a constant rotor angular velocity of $\Omega = 20.94$ rad s⁻¹ was chosen and the freestream velocity was varied to study the effect of advance ratio. During steady rotation at constant angular velocity, the tangential velocity of the wing at the tip was $U_t = 18.62$ m s⁻¹. The freestream velocity had values of $U_\infty = 4.65, 6.70, \text{ and } 7.44$ m s⁻¹, corresponding to three values of advance ratio $\mu = U_\infty/U_t = 0.25, 0.36, \text{ and } 0.4$. The effective velocity U_e of the local wing section is based on the geometry of the flow and given by $U_e = U_t \frac{r}{R} + U_\infty \sin \psi$, where ψ is the azimuth defined in Fig. 1a. The chordwise velocity measurements were acquired at three radial locations $r/R = 0.5, 0.6, \text{ and } 0.7$ and at one azimuthal location

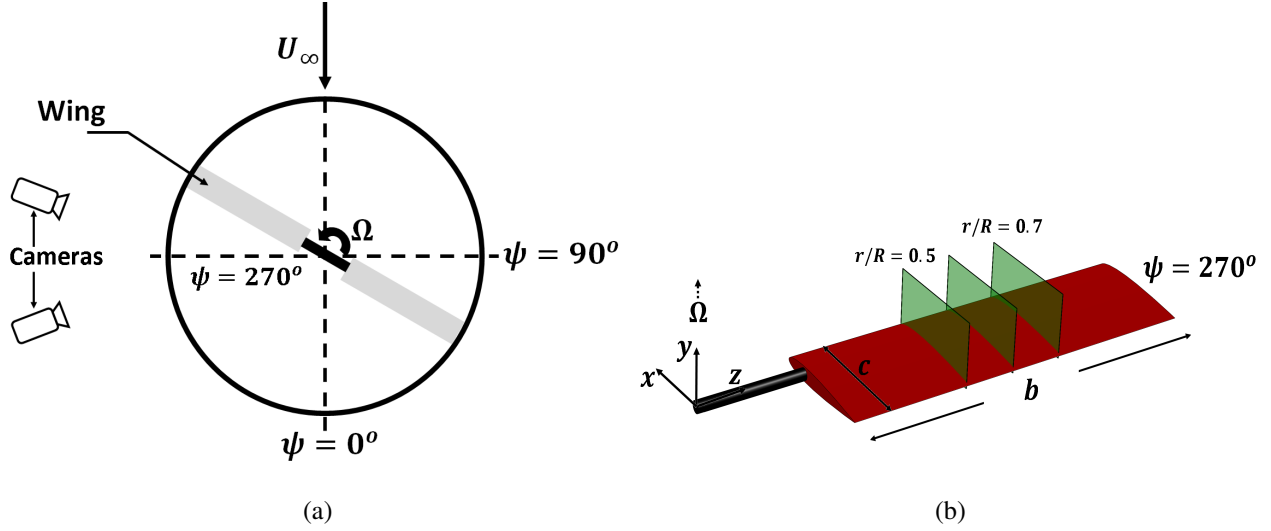


FIG. 1: Schematic of the rotating blade experimental setup and related parameters (not to scale) :
a) Top view defining azimuth ψ and b) Isometric view showing the data measurement locations

μ	0.25	0.36	0.40
r/R			
0.5	52 841	29 591	21 137
0.6	73 978	50 728	42 273
0.7	95 115	71 864	63 410

TABLE I: Reynolds number Re based on chord length and effective velocity at the measurement conditions

$\psi = 270^\circ$ (refer section I for a justification of these measurement locations). The Reynolds number based on chord length and effective velocity $Re = cU_e/\nu$ for each combination of flow condition and measurement location is summarized in table I.

As mentioned earlier the cyclic pitching motion of the blade was achieved by using a swashplate mechanism on the rotor. The pitch angle of the wing as a function of azimuth was manually set to follow the function $\theta(\psi) = \theta_o + \theta_c \sin\psi$, where θ_o is the collective pitch angle and θ_c the cyclic pitch angle. DiOttavio²⁰ determined the collective and cyclic pitch angles needed to induce the formation of a leading edge vortex via dynamic stall on the rotating wing at $\psi = 270^\circ$ for the experimental setup used in this study. Based on that study $\theta_o = 10^\circ$ and $\theta_c = -5^\circ$ were used as

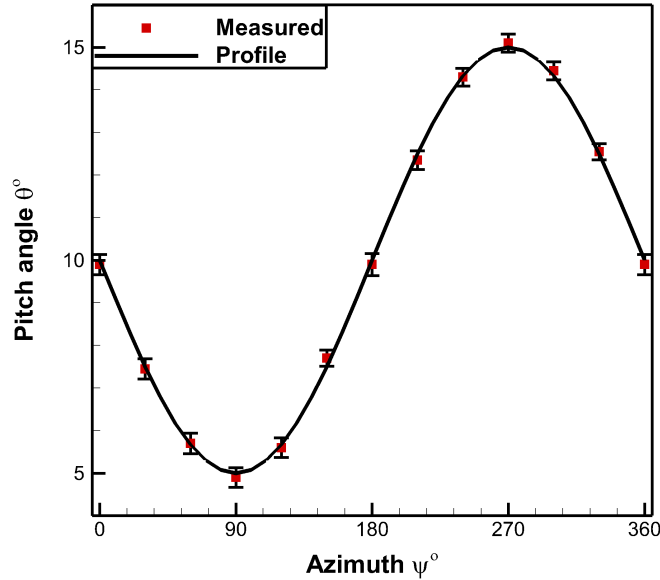


FIG. 2: Plot comparing the prescribed pitch profile to the measurements. The error bars indicate the standard deviation of the pitch angle between different experimental runs.

the pitch settings for all the experiments here. This yields a geometric pitch of 15° at $\psi = 270^\circ$. Before and after each experimental run (total number of experimental runs = 102), the pitch angle was measured using a digital protractor at intervals of $\psi = 30^\circ$ to verify the prescribed pitch angle variation with azimuth. The average of the measurements over the set of all experiments compared to the prescribed profile is summarized in Fig. 2. The error bars indicate the standard deviation of the pitch angles achieved between different experimental runs.

B. SPIV instrumentation

Stereoscopic PIV was used to measure the velocity fields over the rotating blade at $\psi = 270^\circ$. The illumination was provided by a double-cavity Nd:YAG laser with a pulse energy of 200 mJ. A laser arm (a shielded beam path) was used to deliver the laser beam to the measurement planes. Sheet optics were used at the end of the laser arm to generate a light sheet, which was maintained between 1–2 mm in thickness. The flow was continuously seeded with $10\mu\text{m}$ droplets of atomized oil generated by a Laskin-nozzle type aerosol generator. The cameras used for acquiring the images were PRO-X 2M camera systems having a CCD array of 1600×1200 pixels and a pixel size of $7.4 \times 7.4 \mu\text{m}^2$. A lens system with focal length of 50 mm and an aperture setting

of $f/8$ was used with the camera. A series of 75 phase-locked image pairs were acquired in each measurement plane. The number of image pairs to acquire was decided by performing a phase-averaged convergence test to within 0.1% tolerance. The camera calibration was performed using a dual-plane calibration target, and refined using the stereo self calibration technique. DaVis 8.1, a commercially available software, was used to calculate velocities using stereoscopic spatial cross-correlation of the image pairs. A 64×64 pixels interrogation window with 50% overlap and a second interrogation pass with a reduced window size (32×32 pixels) were used to yield a vector spatial resolution of $0.98 - 1.38$ mm ($0.006c - 0.008c$, where c is the chord length) for the measurements. A median filter and light vector smoothing (3×3) were applied in post-processing for better visual presentation. The field of view varied based on the radial location since the lens system had a fixed focal length.

C. Accuracy estimates

The uncertainty in flow conditions arising from velocity, ambient temperature and pressure measurement resulted in a Reynolds number uncertainty of ± 468 . The uncertainty in pitch angle settings measured using a digital protractor and the phase-locking of the rotor estimated by image processing were both determined to be $\pm 0.05^\circ$. Detailed coordinate measurements of the airfoil profile indicated that the root mean square error between the airfoil profile used and a NACA0013 profile was less than 0.1% of the chord length. The accuracy of the velocity measurements was computed using procedures outlined in Raffel²¹. Bias error for in-plane velocity was determined by plotting the probability density histograms of the velocity field data. The histograms had a resolution of 0.01 m s^{-1} and did not reveal any peak-locking error. The lag error for in-plane velocity was estimated to be insignificant by considering the relaxation time of the seed particles to sharp changes in velocity. The random error for in-plane velocity measurement was between 0.4% and 1.2% of the maximum in-plane velocity (12.1 m s^{-1}). Please refer to Raghav⁵ for further details on computation of in-plane velocity measurement uncertainty.

The out-of-plane velocity measurement uncertainty depends on the angle between the two cameras used during SPIV measurements. Lawson²² suggests that the optimal angle is between $20^\circ - 30^\circ$, however, due to limited optical access the angle in this study was limited to 20° . The resulting random error for the out-of-plane velocity measurement was between 0.58% and 3.08% of the maximum out-of-plane velocity (9.1 m s^{-1}). It should be noted that the random errors presented

here are percentages based on the maximum values of two separate velocity components.

III. RESULTS AND DISCUSSION

We present the results under two main categories: the first analysis is performed assuming the existence of a dominant phase-locked average flow field, and the second is conducted to understand the instantaneous flow field. The phase-averaged flow field analysis allows for a generalized study of the effect of advance ratio on the DSV formation. The instantaneous flow field analysis will help quantify the cycle-to-cycle variations and act as an evaluation of the assumption of a dominant phase-average flow field. In all the PIV vector fields presented in this work, the axes of the camera images are fixed in the wind tunnel coordinate system and have not been corrected for the pitch angle of the wing. A right handed axes system with the origin (0,0) at the leading edge of the wing is chosen (see Fig. 1b). The dimensions in x and y are non dimensionalized by chord length c , while the radial dimension r (representing the z dimension in the right hand coordinate system) is non dimensionalized by tip radius R . In order to observe and characterize the vortical structures, the corresponding freestream velocity has been subtracted from the velocity fields.

A. Phase-averaged flow field

1. Structure of the vortex

To effectively characterize the DSV a vortex center identification algorithm proposed by Graftieaux²³ was used to determine the location of the vortex. This method calculates a normalized scalar field Γ_1 also called the normalized angular momentum, which is a measure of the relative rotation about each grid point. This scalar function is capable of characterizing the location of the center of large scale vortical structures by considering only the topology of the flow field. It is specifically designed to identify a large scale vortex superposed on a small-scale turbulent velocity field. The scalar function is defined as

$$\Gamma_1(P) = \frac{1}{N} \sum_S \frac{(PM \wedge U_M) \cdot z}{\|PM\| \cdot \|U_M\|} = \frac{1}{N} \sum_S \sin(\theta_M) \quad (1)$$

where N is the number of points in the two-dimensional neighborhood of S of any given point P in the measurement plane. M lies in S and z is the unit vector normal to the measurement plane. The

parameter N plays the role of a spatial filter, but affects the location of maximum Γ_1 weakly. This scalar function unlike gradient based vortex detection techniques does not require the evaluation of gradients and is hence less susceptible to experimental noise.

A value of $N = 2$ yielded appropriate results with sufficient detail (without smearing/smoothing the boundaries) to discern the DSV as illustrated in Fig. 3. At the most inboard location of $r/R = 0.5$ an increase in advance ratio causes significant changes in the structure of the vortex. For $\mu = 0.36$ and 0.40 a dual vortical structure has developed when compared to the single vortex at the lower advance ratio of $\mu = 0.25$. Furthermore, the dual vortical structure is also observed in its incipient stages of formation at $r/R = 0.6$ and $\mu = 0.40$, where the formation of the secondary vortex from the primary DSV is observed. In the figure, the dual vortical structure is identified by the labels Vortex 1 and Vortex 2. Similar dual vortical structures have also been observed on rotating wings^{2,24} at much lower Reynolds number conditions when compared to this study. From the observations in this work, a trend that arises is that the dual vortical structure exists only at the lower Reynolds number conditions tested (refer to table I for the summary of experimental conditions). Although this is an interesting observation, definitive conclusions cannot be derived from these results since the advance ratio and Reynolds number are not decoupled and hence this needs to be addressed in the future. It could be hypothesized that the formation of the dual vortical structure on a wing undergoing simultaneous rotation and pitching in steady incident tangential flow has an upper Reynolds number limit.

2. *Strength of the vortex*

Having identified salient kinematic features of the DSV, we now quantify the effect of advance ratio by computing the circulation around the vortex. For this purpose an extension of the scalar function Γ_1 , the Γ_2 function proposed by Graftieaux²³ is used to identify the core of the vortex. Γ_2 is a Galilean invariant version in which the previously defined scalar field is modified by taking into account the local advection velocity defined by

$$\Gamma_2(P) = \frac{1}{N} \sum_S \frac{[PM \wedge (U_M - U_P)] \cdot z}{\|PM\| \cdot \|U_M - U_P\|} \quad (2)$$

where $U_P = (1/S) \int_S U dS$ and $|\Gamma_2|$ is bounded by one. Regions where $|\Gamma_2| > 2/\pi$ represent a vortex core. The span-wise vorticity within these regions was summed up to calculate the circulation Γ around the vortex system on the upper surface of the wing. The circulation around the vortex

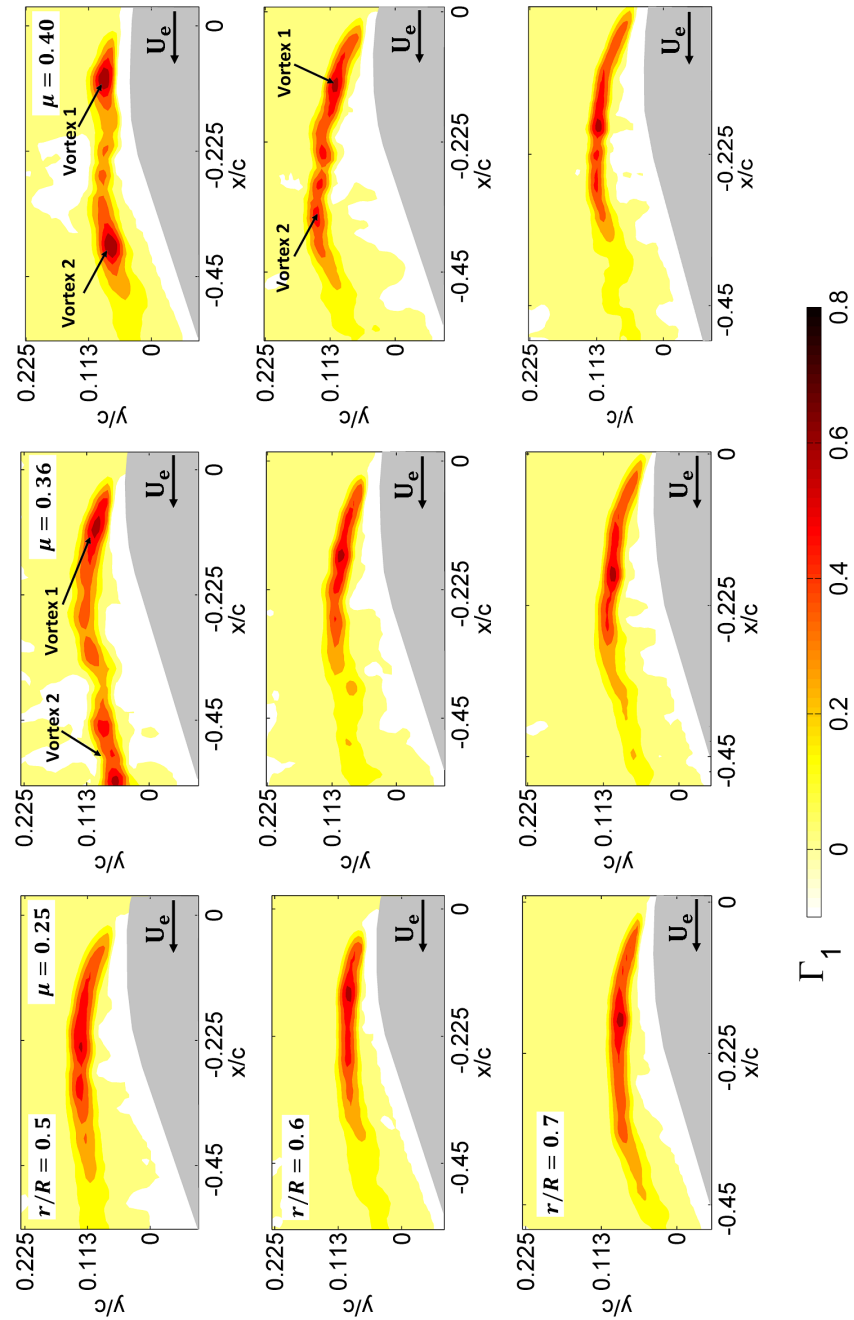


FIG. 3: Γ_1 contours of phase-averaged velocity field illustrating the variation of the flow field with radial location and advance ratio. In each plot, (0,0) is the leading-edge of the rotating wing and the direction of effective velocity U_e is from right to left. The gray portion of the plots is the location of the surface of the wing and laser shadow.

system on the upper surface of the wing was observed to increase on moving outboard. In this work the computed circulation is non-dimensionalized using the chord length c and effective velocity U_e given by $\Gamma^* = \Gamma/cU_e$. This form of non-dimensionalization helps differentiate the strength of the vortex irrespective of the effective freestream responsible for the circulation around the flow field.

The non-dimensional circulation estimates are plotted in Fig. 4a as a function of both radial location as well as advance ratio and Fig. 4b illustrates the variation of the same non-dimensional circulation estimates with Reynolds number. At all the radial locations the non-dimensional circulation around the vortex increases with advance ratio. However, the effect of advance ratio is more pronounced at the inboard location ($r/R = 0.5$) than at the outboard locations. On moving outboard on the wing the non-dimensional circulation decreases consistently across all advance ratios, which indicates that at the inboard locations the vortex is stronger per unit effective velocity. The physical reasoning behind this observation is reconciled later using instantaneous velocity field analysis and vortex stability arguments. The same non-dimensional circulation estimates yield further insight when the variation with Reynolds number is studied. The vortex strength asymptotically approaches a constant at the higher Reynolds numbers as illustrated in Fig. 4b. This variation is related to the formation of the dual vortical structure which was observed to occur at the same lower Reynolds number conditions tested in this work. Furthermore, at the lower Reynolds numbers (where the dual vortical structure was observed) the total circulation around the vortical structures is significantly higher than at the higher Reynolds numbers. This is clear evidence that the circulation around the vortex increased beyond a manageable level, which led the formation (shedding) of a secondary stable DSV (vortex 2). However, as mentioned earlier it should be noted that definitive conclusions cannot be derived from these results since the advance ratio and Reynolds number are not decoupled.

3. Radial flow field

In the rotating environment the coupled effect of centripetal and Coriolis accelerations is expected to create a significant radial velocity field. We now turn our attention to analyze this third component of velocity measured using SPIV. As mentioned earlier, in this study, data were acquired at one particular azimuth ($\psi = 270^\circ$) to focus on the azimuthal location where centripetal acceleration induced radial flow is expected to dominate the flow field. Figure 5 illustrates the ve-

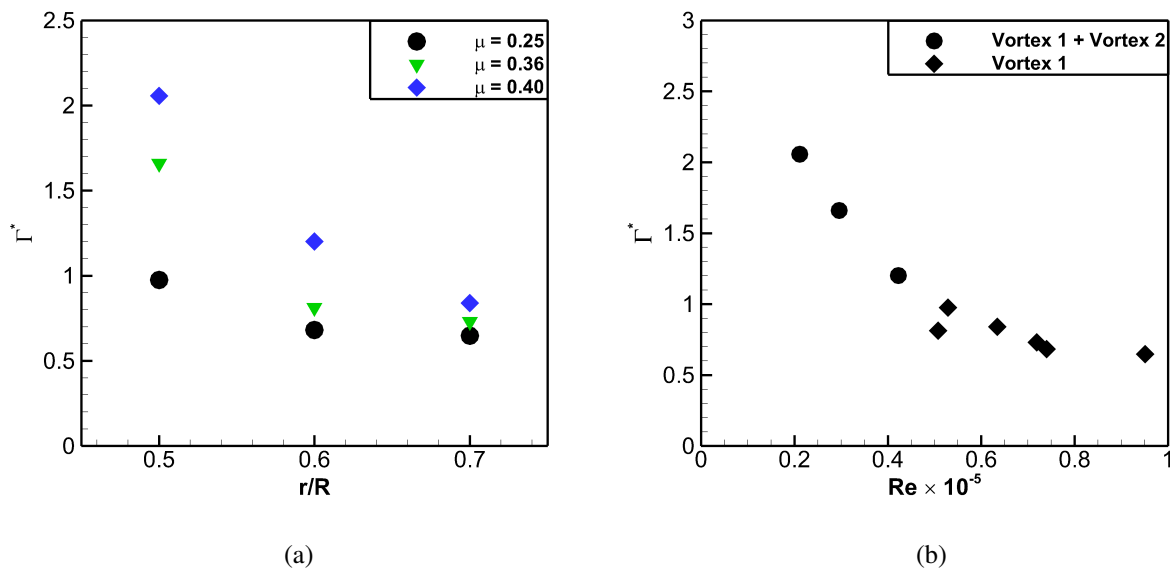


FIG. 4: Non-dimensional circulation around the vortex system on the upper surface of the wing: a) Variation with radial location and advance ratio and b) Variation with Reynolds number - where applicable the circulation around the dual vortical structures has been shown

locity fields represented using streamlines overlaid on contours of normalized radial flow (\bar{w}/U_t) for all the conditions tested in this work. In the illustration the corresponding freestream velocity has been subtracted from the measured velocity vector fields to improve the visualization of the vortices. In all the cases tested, a broad region of positive (root-to-tip) radial flow was observed to extend across the chord of the wing. Mulleners³ also observed similar flow field features on rotating blades in steady forward flight at higher Reynolds numbers. Furthermore, similar flow fields were observed, albeit at much lower Reynolds numbers in experimental investigations by Birch¹¹ and recent numerical computations by Harbig¹³. In addition, the extent of the region of radial flow was observed to have a strong dependence on advance ratio and radial location. While there is some positive velocity within the vortical structures the maximum radial flow in all the cases was located below the center of the vortex closer to the surface of the wing. The maximum radial flow occurring closer to the surface agrees with what one would expect as a radial boundary layer profile similar to that on a rotating disk²⁵.

The radial flow velocity measurements are better visualized by a three-dimensional surface contour plot (please see Fig. 6 for a few selected cases). The surface contours are overlaid on a *representative section* of the wing to elucidate the extent and patterns of radial flow at vary-

Advance ratio effects on the dynamic-stall vortex

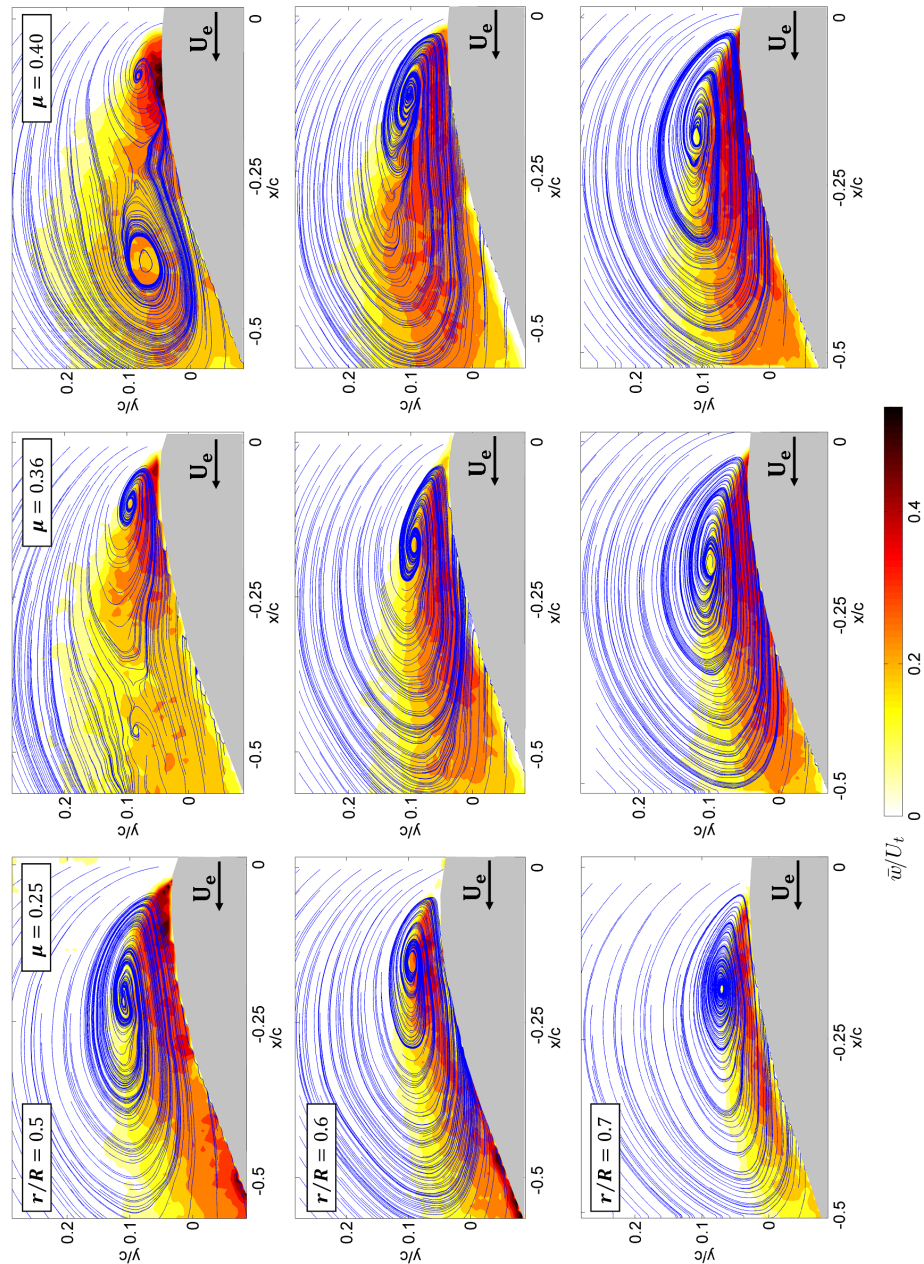


FIG. 5: Streamline plots overlaid on normalized radial velocity \bar{w}/U_t contours illustrating variation with radial location and advance ratio. In each plot, (0,0) is the leading-edge of the rotating wing and the direction of effective velocity U_e is from right to left. The gray portion of the plots is the location of the surface of the wing and laser shadow.

ing advance ratios and radial locations. In these figures the radial velocity data has been lightly smoothed (3×3) for better visual presentation. The three-dimensional nature of the flow field is readily apparent in the figures with the streamlines following the radial flow surface contour.

Advance ratio effects on the dynamic-stall vortex

A feature that stands out is the spatial extent of radial flow over the rotating blade is lower and occurs closer to the leading edge at inboard radial locations ($r/R = 0.5$ see Fig. 6a and Fig. 6b) when compared to the outboard radial locations ($r/R = 0.7$ see Fig. 6c and Fig. 6d). Furthermore, as mentioned earlier the peak radial velocity is typically observed to occur below the center of the vortex, with the radial velocity profile similar to that on a rotating disk. This could imply that the center of the vortex observed in this work is located in the *vicinity* of the inflection point of the radial velocity profile. The implications of this observation is quite interesting but digresses from the main focus of this paper and hence not discussed here.

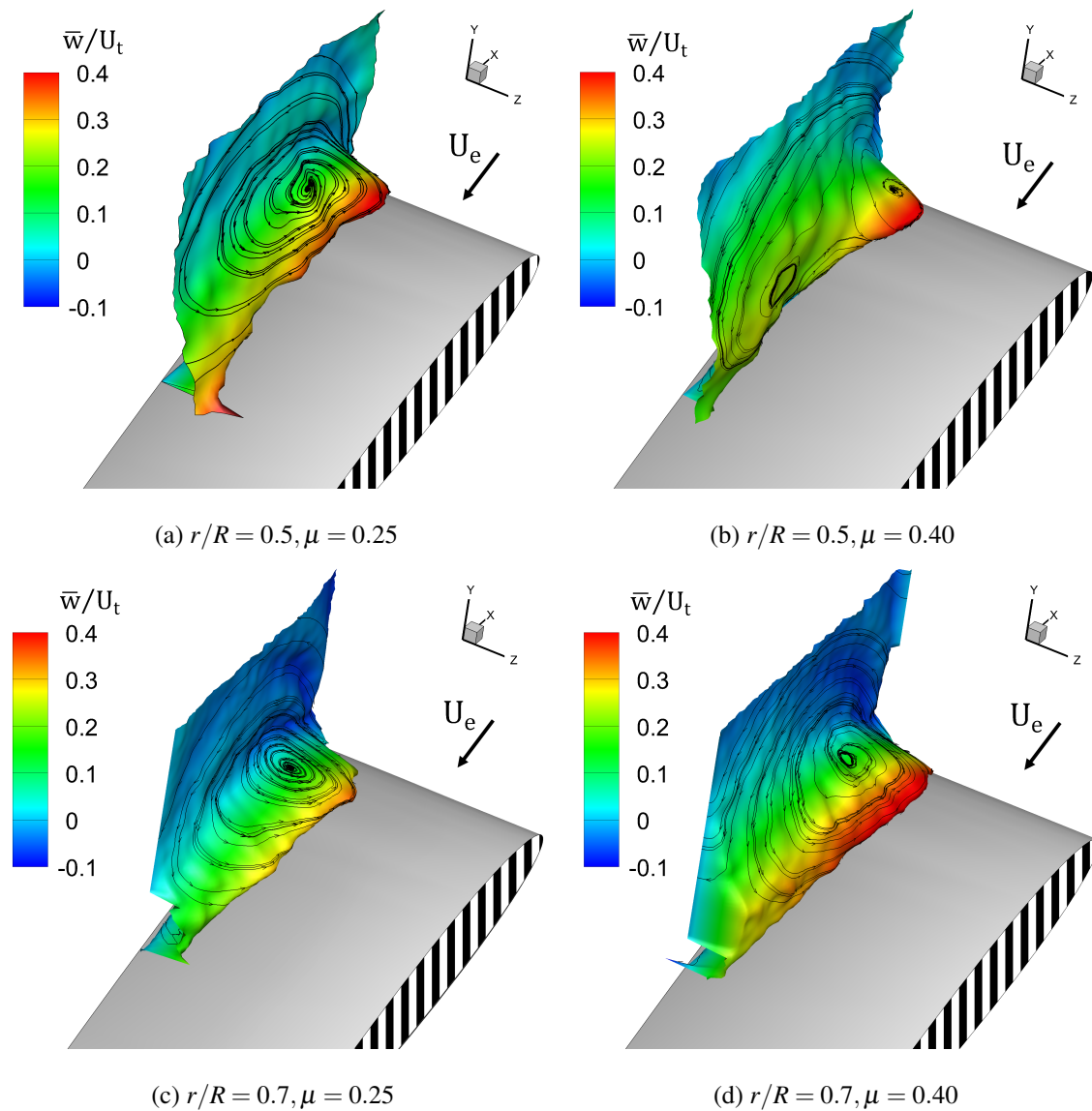


FIG. 6: Streamline plots overlaid on normalized radial velocity \bar{w}/U_t surface contours illustrating variation with radial location and advance ratio.

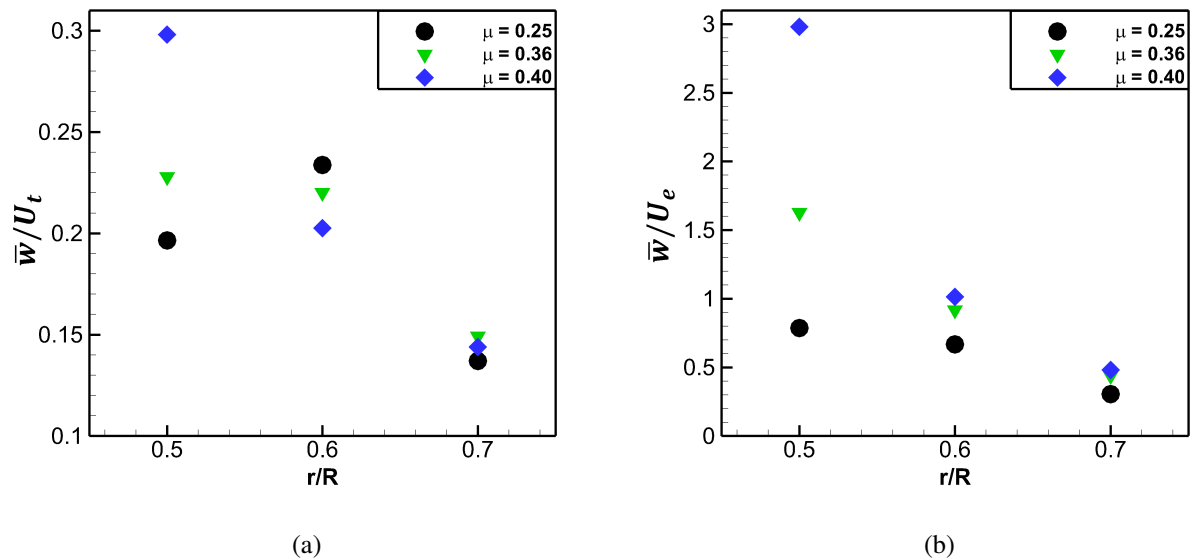


FIG. 7: Radial velocity measured at the center of Vortex 1 : a) Non-dimensionalized by tip velocity and b) Non-dimensionalized by effective velocity

The vortex dynamics of the DSV in the rotating environment is expected to be affected by the radial flow at the core of the vortex. Hence in order to further understand this influence, the phase-averaged radial velocity \bar{w} measured at the center of DSV (identified using the Γ_1 criteria) is presented in Fig. 7, where the positive velocity indicates a root-to-tip flow. Figure 7a illustrates the variation of the radial velocity non-dimensionalized by the tip velocity U_t of the rotating wing. Although no global trend is apparent as advance ratio changes, a salient observation here is the decrease in the radial velocity \bar{w}/U_t at the outboard locations. Although this is in contrast to an expected increase with centripetal acceleration at the outboard locations, it agrees with prior observations by Mulleners³ and Raghav¹⁴. Raghav demonstrated the radial velocity profile on a rotating blade in dynamic stall conditions was susceptible to an apparent shear layer instability. The radial velocity “jet” eventually breaks up into discrete structures, while the peak radial velocity attenuates towards the blade tip. Furthermore, this behavior could be directly related to the existence of a stable DSV based on local Rossby numbers as discussed by Lentink². Based on their discussion, a stable DSV is most likely to occur close to the root of the rotating wing due to lower values of Rossby number, and the flow farther outboard would be unstable. However, the causal effect for the reduction of radial velocity in the core of vortex is yet to be ascertained from further investigations.

If centripetal acceleration alone was responsible for the radial velocity field, one would expect a monotonous change in the peak radial velocity across all advance ratio conditions and radial locations. However, the above observations (Fig. 7a) suggest that there might be another physical mechanism dominating the flow field at the inboard locations, perhaps Coriolis acceleration? In order to further investigate the effect of Coriolis acceleration, the radial velocity is non-dimensionalized by the Coriolis force term $\Omega \times U_e \sim \Omega U_e$. However, since rotation rate Ω is held constant in these experiments, the phase-averaged radial velocity can be non-dimensionalized by the effective velocity U_e . This non-dimensionalization is illustrated in Fig. 7b, where the trends with advance ratio and radial location are clearly evident. At each radial location the radial velocity \bar{w}/U_e increases with advance ratio, however, the increase is around an order of magnitude higher at the inboard locations. The increase in radial velocity with advance ratio at a fixed radial location is quite interesting in that the centripetal acceleration in the flow field has not changed with advance ratio.

Clearly, the role of Coriolis acceleration in the radial flow field is evident in Fig. 7b, since only the Coriolis acceleration changes with advance ratio at a given radial location (due to change in effective velocity). The Coriolis acceleration appears to have a significant effect on the radial flow at the inboard locations with that effect diminishing at the outboard locations. At the outboard locations the centripetal acceleration might have a more significant role on the radial flow than Coriolis acceleration. The role of Coriolis acceleration also ties back to arguments made earlier regarding the effects of a stable DSV based on local Rossby number. A discussion of the effect of radial flow on the stability of the DSV is presented later in section III C.

B. Instantaneous flow field

In this section we present further analysis of the flow field from an instantaneous point of view. This analysis will provide insight into the cycle-to-cycle variations of the DSV over the 75 cycles of data gathered. In order to quantify the cycle-to-cycle variations of the DSV, the variations due to other experimental artifacts have to be quantified. The phase-locking error was quantified by analysing the position of the wing in each SPIV image captured. The root mean square (RMS) error in the position of the wing was less than 0.26% of the chord length. The cycle-to-cycle variation in the onset flow field was computed from the standard deviation of the velocity measured at $\psi = 270^\circ$ when the wing was located at $\psi = 225^\circ$. The standard deviation of 0.10–

0.17 m s^{-1} (2.15–2.28% based on U_∞) indicates an insignificant cycle-to-cycle variation in the onset flow conditions. The above observations isolates the cycle-to-cycle variations observed over the surface of the wing from any variations arising due to geometry of the setup or the incoming steady stream. Hence, any variations observed in the DSV should be only due to the unsteady nature of the three-dimensional flow field.

The analysis of the dominant behavior of a flow field with fine vortical structures superposed on a large scale coherent structure is usually a challenge. An approach to define and identify coherent structures in a complex flow system is based on a proper orthogonal decomposition (POD) of the flow field. The technique denotes a procedure to represent a random spatio-temporal signal as a series of deterministic spatial functions with the temporal function as random coefficients. This modal bi-orthogonal decomposition is then used to approximate the original signal as accurately as possible based on an energy-weighted measure²⁶. DaVis 8.1 software which employs the snapshot technique described by Sirovich²⁷ was used to perform the POD analysis on the velocity fields.

The POD technique was adopted to understand the effect of advance ratio on the dominant flow structure on a rotating wing. Since POD analysis provides an estimate of energy levels, we first present and discuss the effect of advance ratio on the energy distribution between the modes of the flow. The lower modes usually represent the dominant structures of the flow field and are ascribed a higher energy level, while the higher modes represent the finer flow structures in the flow field and are associated with lower energy levels. Figure 8 illustrates the energy contained in each eigenmode of the flow at the measurement location $r/R = 0.6$. The inset is a zoomed in view of the same data to clearly differentiate between the energy levels of the lower modes. A change in advance ratio does not effect the energy content of the higher modes, however, the lower modes show a moderate change (5–10%) with advance ratio. Essentially, a variation in advance ratio affects only the dominant flow structures associated with the lower modes (higher energy levels) rather than the finer scale flow structures which are associated with the higher modes (lower energy levels). Hence, the approximated instantaneous flow field reconstructed using the first 3–4 eigenmodes should be sufficient to draw conclusions on the dominant behavior of the instantaneous flow field.

The unsteadiness of the vortex was characterized by mapping the height y_c between the surface of the wing and the center of vortex 1 in each POD approximated instantaneous flow field. This height was measured for all the flow conditions tested in this work, where the center of the vortex was identified using the Γ_1 criterion. The unsteadiness was quantified by computing the standard

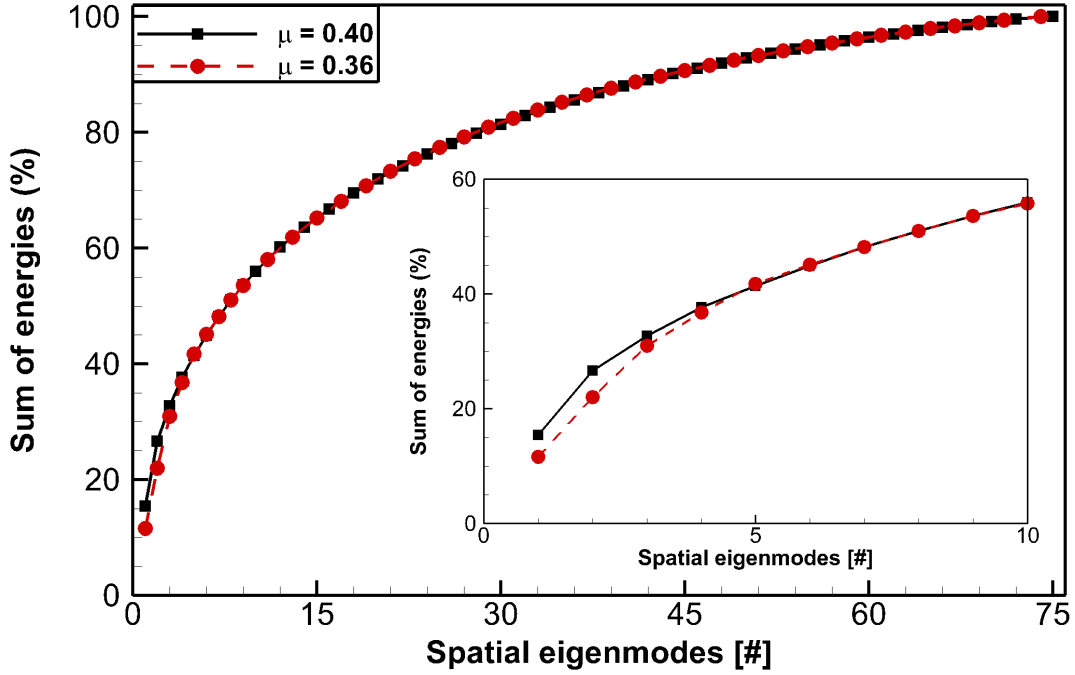


FIG. 8: Sum of energies associated with each eigenmode of the flow at $r/R = 0.6$

deviation of the height y'_c of the center of the vortex at each flow condition, this is plotted in Fig. 9. Although the difference in y'_c values across the experimental conditions appears insignificant, it decides the angle of separated shear layer encompassing the leading-edge vortex. Please refer to supplemental material²⁸ provided as illustrations of sensitivity of the angle of separated shear layer to the height of the center of vortex 1. For example, 10 consecutive instantaneous flow fields at $r/R = 0.5$, $\mu = 0.36$ (Movie 1) and $r/R = 0.6$, $\mu = 0.25$ (Movie 2) indicate a relatively stable vortical structure. However, the consecutive instantaneous flow fields at $r/R = 0.6$, $\mu = 0.36$ (Movie 3) and $r/R = 0.7$, $\mu = 0.40$ (Movie 4) indicate a highly unsteady vortical structure. Hence, y'_c provides a quantitative metric of the cycle-to-cycle unsteadiness in the position of the vortex thereby indicating the stability (tendency to remain attached to the wing) of the DSV. Clearly, there are two regimes of the vortex height variation which are labeled in the figure for clarity. At the most in-board location $r/R = 0.5$ the cycle-to-cycle variation in the position of the vortex does not exhibit any unsteadiness for all advance ratio conditions. At outboard locations $r/R = 0.6, 0.7$ the vortex exhibit significant unsteadiness, which increases with advance ratio. In general, at the outboard locations higher advance ratio tends to create an unsteady vortex.

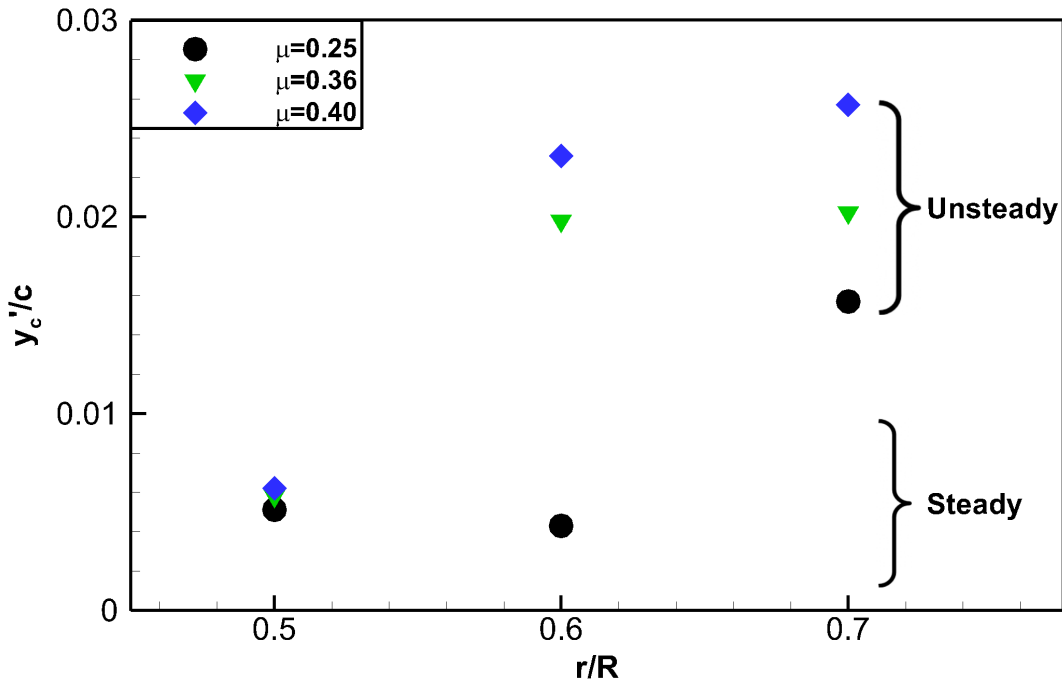


FIG. 9: Cycle-to-cycle variation in the height of the vortex above the surface of the wing illustrating two separate regimes of variation

C. DSV stability

The discussion of cycle-to-cycle unsteadiness of the vortex in the previous section naturally leads into a discussion on its stability. Herein we refer to stability in terms of the unsteadiness of the vortex position. A stable DSV would exhibit relatively steady characteristics and *vice versa*. Although the LEV is essential for an insect to maintain high lift, the shedding of the DSV is an undesirable event on a helicopter rotor and severely limits the performance of the helicopter. Several investigations with two-dimensional and three-dimensional pitching and plunging wings (no rotation) have consistently shown that the DSV is shed after a few chord lengths of travel.

However, investigations that incorporated rotation of the wing have reported a stable DSV at inboard sections (close to the root) on helicopter rotors³⁻⁵ and wind turbine blades⁶. Similar stable vortex structures have been observed on rotating wings at low Reynolds numbers^{2,11}. Lentink² proposed that the centripetal and Coriolis accelerations due to wing rotation mediate a stable LEV. Similarly, Mulleners³ observed that the DSV on a rotating helicopter blade in forward flight was stabilized due to the radial velocity. In this section we address the stability of the DSV observed

in this work with respect to two aspects - the radial flow and advance ratio.

First we discuss the implications of the unexpected decrease in radial velocity at the center of the vortex 1 on the stability of the DSV. Several studies, for example^{9,29} use vorticity transport arguments to postulate that the magnitude of span-wise (radial) velocity is directly related to the size and stability of the DSV. Beem²⁹ argue that a greater magnitude of radial velocity facilitates an equilibrium state through the advection of the vorticity produced at the leading-edge shear layer towards the wing tip. This rapid redistribution of vorticity helps maintain the DSV at a manageable size and therefore stable and attached to the wing. Drawing a parallel to vorticity transport arguments we can now reconcile the possible implications of the observations of radial flow in this work. A reduction in the radial velocity at the core of the DSV is accompanied by a corresponding reduction in the magnitude of the span-wise advection of vorticity. A decrease in advection of vorticity towards the tip of the blade allows the vortex to grow in size and strength, losing its stability. The observation of an unstable vortex at outboard locations is also in agreement with Lentink² who postulated that an unstable LEV exists at high local Rossby numbers (outboard locations on the rotating wing). Using the same definition of local Rossby number as $Ro_l = r/c$, the radial locations tested in this work $r/R = 0.5, 0.6, 0.7$ correspond to $Ro_l = 2.49, 2.99, 3.49$ respectively. Clearly, as Ro_l increases the tendency of the vortex to be unstable is greater as observed in Fig. 9. However, the physics of the instability of the DSV is now traced to the magnitude of radial velocity and the associated span-wise (radial) vorticity transport.

We now shift our attention to the effect of advance ratio on the stability of the DSV. From Fig. 9 it can be observed that at a given outboard radial location an increase in advance ratio results in an unstable vortex. Based on prior literature, the stability of the vortex is characterized based on local Rossby number, however, to account for the effect of advance ratio a universal indicator for the stability of the vortex is necessary. A rigorous form of the local Rossby number defined as $Ro_\mu = (\Omega r - U_\infty)/\Omega c$ could serve as an universal scaling for rotating wings with steady incident tangential flow. Based on the flow conditions this scaling suggests that the critical Rossby number for a stable DSV would be lower than that predicted by local Rossby number as r/c . Figure 10 clearly illustrates that the non-dimensionalized phase-averaged radial velocity \bar{w}/U_e decreases with an increase of Rossby number Ro_μ . Earlier in this section we discussed the implication of reduction of radial flow on the destabilization of the DSV. Reconciling the above two statements we can observe that as Ro_μ increases the vortex tends to destabilize, however, the value at which this destabilization is observed will differ from that predicted by $Ro = r/c$. Further investigations

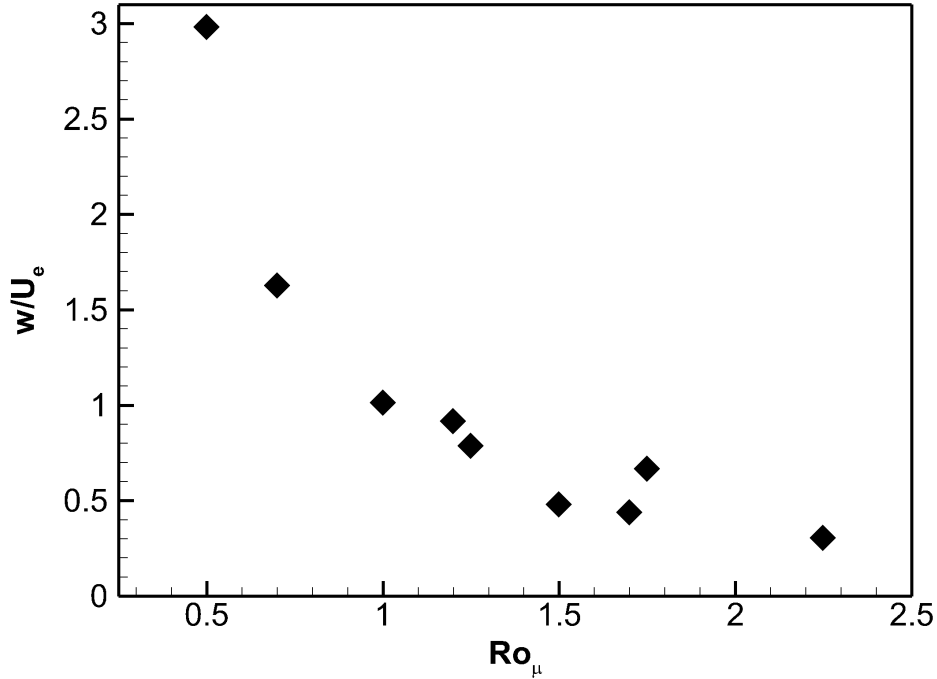


FIG. 10: Variation of non-dimensionalized phase-averaged radial velocity with Rossby number defined to account for advance ratio

are necessary to rigorously define the local Rossby number Ro_μ and a critical value under steady forward flight conditions.

IV. CONCLUSIONS

The flow structure on a simultaneously rotating and pitching blade in steady forward flight was characterized with respect to advance ratio and radial location. Advance ratio greatly affected the flow structure based on the radial location. At inboard radial locations (corresponding to the lower Reynolds number conditions) the DSV was observed to split into two stable vortical structures. However, the dual vortical structure was not observed at the outboard locations (corresponding to higher Reynolds number conditions) suggesting an upper Reynolds number bound on the formation of such stable dual vortical structures. The non-dimensional circulation estimate indicates a strong dependence on advance ratio at the inboard locations and a weaker dependence on advance ratio at the outboard locations. The vortex strength also asymptotically approaches a constant on increasing the Reynolds number of the flow condition. This variation is related to the formation of

the dual vortical structure only at the lower Reynolds number conditions.

The regional extent of positive radial flow (root-to-tip) was observed to increase with the advance ratio at a fixed radial location and decrease on moving outboard at a fixed advance ratio. The increase in phase-averaged radial velocity at the center of vortex 1 with advance ratio at a fixed radial location is clear evidence of the role of Coriolis acceleration in the radial flow field. Furthermore, the phase-averaged radial velocity at the center of vortex 1 was observed to decrease on moving outboard, which is a striking observation in contrast to an expected increase with centripetal acceleration at the outboard locations. The causal effect for the reduction of radial velocity in the core of the vortex is yet to be ascertained from time resolved velocity measurements.

A change in advance ratio affects only the dominant flow structures associated with the lower modes (higher energy levels) rather than the finer scale flow structures which are associated with the higher modes (lower energy levels). POD based analysis of the cycle-to-cycle variations indicated a clear dependence on the local Rossby number $Ro_l = r/c$, with the unsteadiness increasing at high Ro_l . Additionally, at high Ro_l conditions an increase in advance ratio results in an unsteady vortex.

The radial flow plays a critical role in achieving an equilibrium state through the advection of the vorticity produced at the leading-edge shear layer towards the wing tip. The decrease in radial flow at outboard locations inhibits the equilibrium state through a reduction in advection of vorticity towards the blade tip. Hence this unexpected decrease in radial flow can be argued to greatly affect the DSV with respect to attachment and stability. At the inboard location $r/R = 0.5$ the vortex was stable and insensitive to change in advance ratio. However, at the outboard location $r/R = 0.6, 0.7$ the stability of the vortex was observed to be sensitive to advance ratio, with high advance ratios resulting in an unstable vortex.

ACKNOWLEDGMENTS

This research program was funded by the Army Research Office (ARO), grant number: W911NF1010398, with Dr. Bryan J. Glaz as the program manager. The authors acknowledge the assistance of Alex Forbes, Brandon Liberi, and Sorin Pirau with the experimental setup and measurements, and the assistance of Nicholas Motahari with the post processing of data.

REFERENCES

- ¹W. Dickson and M. Dickinson, “The effect of advance ratio on the aerodynamics of revolving wings,” *Journal of Experimental Biology* **207**, 4269–4281 (2004).
- ²D. Lentink and M. Dickinson, “Rotational accelerations stabilize leading edge vortices on revolving fly wings,” *Journal of Experimental Biology* **212**, 2705–2719 (2009).
- ³K. Mulleners, K. Kindler, and M. Raffel, “Dynamic stall on a fully equipped helicopter model,” *Aerospace Science and Technology* **19**, 72–76 (2012).
- ⁴F. De Gregorio, K. Pengel, and K. Kindler, “A comprehensive piv measurement campaign on a fully equipped helicopter model,” *Experiments in fluids* **53**, 37–49 (2012).
- ⁵V. Raghav and N. Komerath, “Velocity measurements on a retreating blade in dynamic stall,” *Experiments in Fluids* **55:1669**, 1–10 (2014).
- ⁶J. Tangler, “Insight into wind turbine stall and post-stall aerodynamics,” *Wind Energy* **7**, 247–260 (2004).
- ⁷C. S. Ferreira, G. van Kuik, G. van Bussel, and F. Scarano, “Visualization by piv of dynamic stall on a vertical axis wind turbine,” *Experiments in Fluids* **46**, 97–108 (2009).
- ⁸H. Lee and Y. Wu, “An experimental study of stall delay on the blade of a horizontal-axis wind turbine using tomographic particle image velocimetry,” *Journal of Wind Engineering and Industrial Aerodynamics* **123**, 56–68 (2013).
- ⁹C. Ellington, C. Van Den Berg, A. Willmott, and A. Thomas, “Leading-edge vortices in insect flight,” *Nature* **384**, 626–630 (1996).
- ¹⁰J. Birch and M. Dickinson, “Spanwise flow and the attachment of the leading-edge vortex on insect wings,” *Nature* **412**, 729–733 (2001).
- ¹¹J. Birch, W. Dickson, and M. Dickinson, “Force production and flow structure of the leading edge vortex on flapping wings at high and low reynolds numbers,” *Journal of Experimental Biology* **207**, 1063–1072 (2004).
- ¹²C. Ozen and D. Rockwell, “Three-dimensional vortex structure on a rotating wing,” *Journal of Fluid Mechanics* **707**, 541 (2012).
- ¹³R. Harbig, J. Sheridan, and M. Thompson, “Reynolds number and aspect ratio effects on the leading-edge vortex for rotating insect wing planforms,” *Journal of Fluid Mechanics* **717**, 166–192 (2013).
- ¹⁴V. Raghav and N. Komerath, “An exploration of radial flow on a rotating blade in retreating

- blade stall,” *Journal of the American Helicopter Society* **58**, 1–10 (2013).
- ¹⁵F. Caradonna and C. Tung, “Experimental and analytical studies of a model helicopter rotor in hover,” TM 81232 (NASA, 1981).
- ¹⁶G. Srinivasan, V. Raghavan, E. Duque, and W. McCroskey, “Flowfield analysis of modern helicopter rotors in hover by navier-stokes method,” *Journal of the American helicopter society* **38**, 3–13 (1993).
- ¹⁷M. Raffel, H. Richard, K. Ehrenfried, B. Van der Wall, C. Burley, P. Beaumier, K. McAlister, and K. Pengel, “Recording and evaluation methods of piv investigations on a helicopter rotor model,” *Experiments in Fluids* **36**, 146–156 (2004).
- ¹⁸M. Bross, C. Ozen, and D. Rockwell, “Flow structure on a rotating wing: Effect of steady incident flow,” *Physics of Fluids (1994-present)* **25**, 081901 (2013).
- ¹⁹W. Johnson, *Helicopter theory* (Courier Dover Publications, 2012).
- ²⁰J. DiOttavio, K. Watson, J. Cormey, N. Komerath, and S. Kondor, “Discrete structures in the radial flow over a rotor blade in dynamic stall,” in *Proceedings of the 26th applied aerodynamics conference, AIAA, Honolulu, Hawaii, USA* (2008).
- ²¹M. Raffel, C. Willert, and J. Kompenhans, *Particle Image Velocimetry: A Practical Guide* (Springer, 1998).
- ²²N. Lawson and J. Wu, “Three-dimensional particle image velocimetry: experimental error analysis of a digital angular stereoscopic system,” *Measurement Science and Technology* **8**, 1455 (1997).
- ²³L. Graftieaux, M. Michard, and N. Grosjean, “Combining PIV, POD and vortex identification algorithms for the study of unsteady turbulent swirling flows,” *Measurement Science and Technology* **12**, 1422 (2001).
- ²⁴Y. Lu, G. Shen, and G. Lai, “Dual leading-edge vortices on flapping wings,” *Journal of experimental biology* **209**, 5005–5016 (2006).
- ²⁵V. Kármán, “Über laminare und turbulente reibung,” *ZAMM-Journal of Applied Mathematics and Mechanics/Zeitschrift für Angewandte Mathematik und Mechanik* **1**, 233–252 (1921).
- ²⁶N. Aubry, R. Guyonnet, and R. Lima, “Spatiotemporal analysis of complex signals: theory and applications,” *Journal of Statistical Physics* **64**, 683–739 (1991).
- ²⁷L. Sirovich, “Turbulence and the dynamics of coherent structures. i-coherent structures. ii-symmetries and transformations. iii-dynamics and scaling,” *Quarterly of applied mathematics* **45**, 561–571 (1987).

Advance ratio effects on the dynamic-stall vortex

²⁸See supplementary material at [URL will be inserted by AIP] for videos that show examples of sensitivity of the angle of separated shear layer to the height of the center of vortex 1.,

²⁹H. Beem, D. Rival, and M. Triantafyllou, “On the stabilization of leading-edge vortices with spanwise flow,” *Experiments in fluids* **52**, 511–517 (2012).